Computers and Geotechnics 183 (2025) 107218

Contents lists available at ScienceDirect

Computers and Geotechnics

journal homepage: www.elsevier.com/locate/compgeo

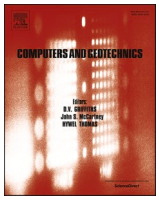

Enhanced elastoplasticity-based frictional-collisional model for solid–fluid phase transition of granular media

Hang Feng [a], Zhen-Yu Yin [a,b,*]

[a] Department of Civil and Environmental Engineering, The Hong Kong Polytechnic University, Hung Hom, Kowloon, Hong Kong, China
[b] Research Institute for Land and Space, The Hong Kong Polytechnic University, Hung Hom, Kowloon, Hong Kong, China

ARTICLE INFO

Keywords:
Granular soil
Constitutive model
Elastoplasticity
Viscosity
Phase transition

ABSTRACT

Accurately describing the solid-like and fluid-like behaviors of granular media is crucial in geotechnical engineering. While the unified frictional-collisional model, integrating rate-independent frictional and rate-dependent collisional stresses, is widely used for solid–fluid phase transitions, an effective model is still under investigation, and comprehensive analyses are lacking. This study addresses these gaps by developing an enhanced elastoplasticity-based frictional-collisional model. The frictional stress is modeled using a critical-state-based elastoplasticity approach, and the collisional stress is formulated through an enhanced kinetic theory incorporating particle stiffness. Subsequently, comprehensive element simulations are conducted to explore the effects of concentration, particle stiffness, and strain rate paths on the model. The proposed model's effectiveness is also validated against experimental data. Finally, a detailed comparison with the typical μ(I) rheology model and a state-equation-based phase transition model is conducted. Our analyses show that the developed model effectively captures strain rate path and particle stiffness through the collisional stress component, while concentration-dependent characteristics are captured through both frictional and collisional stress components. Through comparative analyses, we also found that both the state-equation-based and elastoplasticity-based models depict solid-like behavior and replicate the rheology of granular media in a fluid-like state, similar to the μ(I) model. However, they differ in implementing critical state theory: the state-equation-based model acts as a partial-range phase transition model, describing stress evolution from the critical state to the fluid-like state, while the proposed elastoplasticity-based model serves as a full-range phase transition model, covering stress evolution from the initial to the fluid-like state.

1. Introduction

Granular media, an assemblage of discrete solid particles, exhibit multifaceted and intricate behaviors. For instance, sand may behave in a flow-like state on a beach or desert but demonstrate solid-like behavior when used as a foundation for buildings or streets. It can even exhibit gas-like behavior, as Jaeger et al. (1996) reported. Specifically, granular matter in the solid-like state displays peculiar mechanical properties such as compressive behavior (e.g., an increase in elastic modulus under increasing pressure), shear behavior (e.g., the friction-yielding property during shearing), and the stress-dilatancy (e.g., the volumetric strain increases or decreases under the effect of the shear stress) (Yin et al. 2020). While in the fluid-like state, it becomes highly dependent on the loading rate, featuring strong viscous behavior (Bagnold 1954; Luding 2016). When granular material is gas-like, inelastic collisions dominate the dynamics (Garzó and Dufty, 1999). These extraordinary and complicated mechanical responses present a challenge to accurately describe the granular media.

Various theoretical approaches have been developed to describe the intricate mechanical behaviors of granular media. For the solid-like state, a range of constitutive models has been developed in the geotechnical field, including the elastoplastic framework (e.g., Drucker and Prager, 1952; Wood, 1990; Huang et al., 2018; Yin et al.,2020; Feng et al., 2024b, 2024a), hypoplasticity models (e.g., Wu and Bauer, 1994; Wu et al., 2017), multiscale modeling theories (e.g., Nicot and Darve, 2005), and data-driven approaches (e.g., Zhang et al., 2020; Zhang et al., 2021), to describe the sophisticated responses of granular matter in the solid-like state. In the gas-like state, the kinetic theory has been proposed to describe the collisional mechanism (e.g., Savage, 1984; Lun, 1991; Garzó and Dufty, 1999; Jenkins and Zhang, 2002). For the

* Corresponding author.
E-mail addresses: 23039257r@connect.polyu.hk (H. Feng), zhenyu.yin@polyu.edu.hk (Z.-Y. Yin).

https://doi.org/10.1016/j.compgeo.2025.107218
Received 23 January 2025; Received in revised form 7 March 2025; Accepted 17 March 2025
Available online 27 March 2025

fluid-like state, phenomenological rheology models (e.g., Da Cruz et al., 2005; Daniel et al., 2007; Jop et al., 2006) have been developed, with the widely adopted μ(I) model capturing fluid-like rheology through three non-dimensional parameters: concentration, shear-to-normal stress ratio, and the inertial parameter, which represents the ratio of time scales associated with motion perpendicular and parallel to the flow (MiDi, 2004 Jop et al., 2006). Despite these advances, capturing both solid-like and fluid-like behaviors within a unified framework remains a significant challenge. This challenge is particularly relevant to geotechnical engineering, as granular flows in natural hazards, such as fluid-like landslides, involve a transition from a solid-like to a fluid-like state.

In the literature, many models have been developed to describe the solid–fluid phase transition in granular materials. These include: (i) models incorporating the rheological relation into the elastoplastic framework (e.g., Kamrin, 2010; Dunatunga and Kamrin, 2015; Baumgarten and Kamrin, 2019; Dunatunga and Kamrin, 2022 ; Zhu et al., 2022); (ii) models combining elastic stress and kinetic stress using the MiDi rheological relation (Fei et al., 2016); (iii) models based on hydrodynamic formulations integrated with plasticity theory (Alaei et al., 2021); and (iv) unified frictional-collisional models that decompose granular stress into rate-independent frictional and rate-dependent collisional components (e.g., Savage, 1984; Johnson and Jackson, 1987, Johnson et al., 1990; Berzi et al., 2011; Vescovi et al., 2013; Redaelli et al., 2016; Redaelli et al., 2019; Marveggio et al., 2022; Peng et al., 2016; Guo et al., 2021; Wang and Wu, 2024). Due to the simple framework and clear mechanical mechanism of the last model, we adopt and discuss this approach in this study.

The unified frictional-collisional model, initially developed by Johnson and Jackson (1987, 1990), combined rate-independent frictional stress, generated from force chains among particles, with rate-dependent collisional stress derived from the kinetic theory for dilute flows. Despite its innovation, the model's reliance on the dilute flow assumption limited its applicability to dense granular systems. To address this, Berzi et al. (2011) and Vescovi et al. (2013) employed the extended kinetic theory (see Vescovi, 2014) to describe dense granular flows, integrating the Mohr-Coulomb criterion within the critical state framework (Roscoe et al., 1963; Schofield and Wroth, 1968) for frictional stress. This advancement laid the groundwork for modeling solid–fluid phase transitions. Subsequently, Redaelli et al. (2016) adopted the extended kinetic theory for collisional stress while implementing a standard elastoplastic model with the critical state concept for frictional stress. Building on this, Marveggio et al. (2022) introduced kinematic hardening into the elastoplastic framework. More recently, Wu et al. (2020) proposed various solid–fluid phase transition models, replacing kinetic theory with phenomenological rheology models to describe rate-dependent stress and employing a critical-state-based hypoplastic model to characterize the rate-independent stress. These include the hypoplasticity-Bagnold model (Peng et al., 2016; Guo et al., 2021) and the hypoplasticity-μ(I) model (Wang and Wu, 2024).

Building on the concept of the unified frictional-collisional model, our group has proposed a phase transition model integrating a critical-state-based elastoplasticity framework with the kinetic theory (Feng et al., 2025). However, this model employs collisional stress with rigid granular particles, failing to account for particle stiffness during the collisional mechanism. The influence of particle stiffness on granular flow behavior has been investigated through experimental and discrete element simulation studies. Experiments on concentrated suspensions of hard and rigid particles have shown distinct differences in the straining and flow behavior between suspensions of hard and soft spheres, particularly in unsteady regimes. This is attributed to the development of permanent contacts among deformable spheres (Van der Vaart et al., 2013). Numerical studies, such as those by Brewster et al. (2008) and Bharathraj and Kumaran (2018), also demonstrate that particle stiffness significantly affects the rheology of granular flows. Importantly, Singh et al. (2015) found that both the effective stress and the friction coefficient (the ratio of shear to mean stress) increase with particle stiffness. These findings are linked to micro-collisional mechanisms, where particle stiffness influences the contact duration during collisions (Berzi and Jenkins, 2015) and allows particles to deform, achieving steady shear in dense configurations (Vescovi and Luding, 2016). These observations highlight the importance of incorporating particle stiffness into existing unified frictional-collisional models to more accurately describe granular behavior in the collisional regime.

Additionally, a comprehensive analysis of the unified frictional-collisional model is still lacking. Several important aspects remain unresolved, including the evolution of granular temperature during simulations, the model's ability to capture the effects of strain rate path and initial concentration, and the differences between the proposed model and existing frictional-collisional models and typical μ(I) rheology model.

To address these issues, this study, building upon our previous work (Feng et al., 2025), aims to conduct a comprehensive constitutive analysis by employing an enhanced unified elastoplasticity frictional-collisional model that incorporates a modified kinetic theory considering particle stiffness. The basic structure of the paper is as follows: Section 2 introduces the proposed enhanced elastoplasticity-based phase transition model, followed by an evaluation of the model in Section 3. Section 4 further verifies the proposed model by simulating experimental data. Section 5 presents the comprehensive comparative analysis with simulation results from a typical μ(I) rheology model and a state-equation-based phase transition model. Finally, Section 6 summarizes the main conclusions.

2. Proposed elastoplasticity-based phase transition model

This section discusses the basic framework of the unified frictional-collisional phase transition model and proposes a new elastoplasticity-based phase transition model that combines the critical-state-based elastoplasticity and the modified kinetic theory considering particle stiffness.

2.1. Basic framework

As suggested by Johnson et al. (1990), Johnson and Jackson (1987) and Jaeger et al. (1996), the energy of granular media under external force is dissipated through frictional and collisional mechanisms. Based on this physical principle, a superposition concept is introduced to describe the solid-like and fluid-like behaviors of granular media, as shown in Eq. (1). The total stress in granular flow can be divided into rate-independent frictional stress $\boldsymbol{\sigma}_f$ and rate-dependent collisional stress $\boldsymbol{\sigma}_{col}$. Frictional stress primarily arises from force chains through particle contacts, while collisional stress is mainly generated via the collisional mechanism. Accordingly, a capable model that describes the solid-like and fluid-like behaviors of granular flows in a unified manner should satisfy two criteria: (i) In the small strain range, the frictional stress should dominate, indicating a solid-like state, while collisional stress remains negligible; (ii) In the large strain rate range, the collisional stress should dominate, indicating a fluid-like state, while frictional stress remains negligible.

$$\sigma = \sigma_f + \sigma_{col} \tag{1}$$

where $\boldsymbol{\sigma}$ is the total stress tensor, $\boldsymbol{\sigma}_f$ is the frictional stress; $\boldsymbol{\sigma}_{col}$ is the collisional stress.

2.2. Critical-state-based elastoplasticity for frictional stress

When granular media is in a solid-like state, its behavior is primarily governed by frictional mechanisms, exhibiting frictional yielding characteristics. To describe this solid-like behavior, a critical-state-based elastoplastic model is employed (see Yin et al., 2020; Feng et al.,

2025). This frictional stress model effectively captures the solid-like responses of granular media up to the critical state. Key factors including nonlinear elasticity, nonlinear plastic hardening, stress dilatancy (contraction or dilation), and the critical-state concept, are incorporated into the model. In our study, the critical state concept aligns with that used in soil mechanics. This state refers to a condition where the frictional stress and volume of geomaterials remain constant with continuous shear strain (Roscoe et al., 1963; Schofield and Wroth, 1968). Specifically, at the critical state, the frictional stress remains unchanged, and the granular media enters the fluid-like state from the solid-like state.

The effectiveness of this model in capturing frictional stress during the solid–fluid phase transition has been thoroughly validated through a series of element tests conducted by Feng et al. (2025). The parameters of the critical-state-based elastoplastic frictional stress model are summarized in Table 1. This section omits the details of the elastoplastic stress model, as a comprehensive discussion is provided in Appendix A.

2.3. Modified kinetic theory for collisional stress

When granular media transition to the fluid-like state, their behavior is predominantly governed by the collisional mechanism, resembling the characteristics of viscous fluids. The collisional stress in this state is effectively described by the kinetic theory of granular gases (Garzó and Dufty, 1999; Jenkins and Zhang, 2002; Vescovi, 2014), which is analogous to the kinetic theory of molecular gases. This theory introduces the concept of granular temperature, analogous to the thermodynamic temperature of gases, to quantify particle velocity fluctuations and the level of agitation within the granular system (Goldhirsch, 2008). This section provides a brief overview of the collisional stress as described by kinetic theory for the sake of completeness, with further details available in Vescovi (2014).

Table 1
Input parameters in the proposed elastoplasticity-based phase transition model.

Stress	Symbol	Parameter	Analysis	Polystyrene beads	Glass beads
$\boldsymbol{\sigma}_{col}$	ρ_p	Particle density (kg/m^2)	2000	1050	2970
	d	Diameter (m)	1•10^{-3}	1•10^{-3}	1.8•10^{-3}
	Φ_s	Void ratio parameter	0.55	0.52	0.62
	Φ_m	Volume fraction parameter	0.4	0.4	0.4
	ε_r	Effective restitution coefficient	0.6	0.7	0.6
	E_p	Particle's Young's modulus (Pa)	3•10^6	3•10^9	70•10^9
$\boldsymbol{\sigma}_f$	E_0	Dimensionless referential elastic modulus	100	190	200
	ν	Poisson's ratio	0.200	0.235	0.235
	p_{at}	Atmospheric pressure (kPa)	101.3	101.3	101.3
	n	Parameter of nonlinear elasticity	0.6	0.6	0.6
	φ	Critical-state friction angle	10	23	25
	e_{ref}	Initial critical-state void ratio	0.907	0.910	0.917
	λ	Parameter of CSL	0.122	0.122	0.122
	ξ	Parameter of CSL	0.71	0.71	0.71
	A_d	Stress dilatancy constant	0.5	0.5	0.5
	k_p	Plastic modulus-related constant	0.022	0.001	0.001
	n_p	Interlocking related peak strength parameter	1	1	1
	n_d	Interlocking related phase transformation parameter	1	1	1

The constitutive relation for collisional stress is expressed in Eq. (2), which shares a similar form with the relations used for viscous fluids.

$$\sigma_{col} = \boldsymbol{p}_{col}\delta_{ij} - 2\eta_v\left(\dot{\boldsymbol{e}}_{ij} - \frac{1}{3}\delta_{ij}\nabla\cdot\boldsymbol{u}\right) - \gamma_v(\nabla\cdot\boldsymbol{u})\delta_{ij} \tag{2}$$

where $\dot{\boldsymbol{e}}_{ij}$ is the strain rate tensor; δ_{ij} is the Kronecker's symbol; $\boldsymbol{p}_{col}$, η_v, and γ_v denote the collisional hydrostatic stress, shear viscosity, and bulk viscosity, respectively; expressed as follows:

$$\boldsymbol{p}_{col} = 4G(\Phi)F(\Phi,\varepsilon_n)\rho T \tag{3}$$

$$\eta_v = \frac{8}{5\sqrt{\pi}}G(\Phi)J(\Phi,\varepsilon_n)\rho d T^{0.5} \tag{4}$$

$$\gamma_v = \frac{4}{3\sqrt{\pi}}G(\Phi)Q(\Phi,\varepsilon_n)\rho d T^{0.5} \tag{5}$$

where Φ is the volume fraction of granular medium, related to the void ratio e via $\Phi = 1/(1+e)$; ρ is the density of the granular medium, related to the particle density ρ_p via $\rho = \Phi\,\rho_p$. T is the granular temperature of the granular medium, quantifying particle velocity fluctuation; d is the diameter of the granular particle; ε_n is the restitution coefficient, depicting the restitution during the collision; F, J, and Q are auxiliary functions determined by the volume fraction and restitution coefficient ε_n (refer to Appendix B); $G(\Phi)$ is a function of the volume fraction, determined by $G(\Phi) = \Phi g_0(\Phi)$ (where $g_0(\Phi)$ is the radial distribution function).

The radial distribution function $g_0(\Phi)$ can be represented by various expressions, including those proposed by Carnahan and Starling (1969), Torquato (1995), and Vescovi (2014). This study considers the expression by Vescovi (2014), which is presented as follows:

$$g_0(\Phi) = f(\Phi)\frac{2-\Phi}{2(1-\Phi)^3} + (1-f(\Phi))\frac{2}{\Phi_s-\Phi} \tag{6}$$

$$f(\Phi) = \begin{cases} 1 & \text{if}(\Phi < \Phi_m) \\ \dfrac{\Phi^2 - 2\Phi_m\Phi + \Phi_s(2\Phi_m - \Phi_s)}{2\Phi_s\Phi_m - \Phi_m^2 - \Phi_s^2} & \text{otherwise} \end{cases} \tag{7}$$

where Φ_s is the densest possible disordered configuration during the granular flow and represents the maximum volume fraction for collisional stress; Φ_m is a function parameter and can take the value of 0.4 for steady shear flow.

The restitution coefficient ε_n is originally derived without considering the friction during the collision. To incorporate the frictional effect, it can be replaced by the effective coefficient ε_r, as described by Jenkins and Zhang (2002) and Chialvo et al. (2012). Herein a simple form by Chialvo et al. (2012) is adopted:

$$\varepsilon_r = \varepsilon_n - \frac{3}{2}\mu_p\exp\left(-3\mu_p\right) \tag{8}$$

where μ_p is the friction coefficient, typically taking the value of 0–0.5.

The granular temperature T, which describes the velocity fluctuation of granular particles, can be derived from the fluctuating energy balance:

$$\boldsymbol{\sigma}_{\text{col}} : \dot{\varepsilon} = \frac{3}{2}\rho\dot{T} + \nabla\cdot\boldsymbol{q}_{col}^E + \Gamma_{col} \tag{9}$$

where $\boldsymbol{q}_{col}^E$ is the divergence of the flux of energy, expressed via Eq. (10); Γ_{col} is the collisional dissipated energy, expressed via Eq. (10).

$$\boldsymbol{q}_{col}^E = -\kappa\nabla T - \mu\nabla\rho \tag{10}$$

$$\Gamma_{col} = \frac{144}{5\sqrt{\pi}} \frac{\rho}{d} \frac{T^{3/2}\zeta^*}{(1+e)} \tag{11}$$

where κ is the thermal conductivity; μ is the coefficient of the density gradient; ζ^* is the auxiliary function (refer to Appendix B).

The aforementioned collisional stress has been validated as an effective tool for modeling collisional stress in the solid–fluid phase transition of granular flow, as demonstrated in our previous research (see Feng et al., 2025). However, the original theory does not consider particle stiffness and presents a complex formulation. Therefore, related modifications are being proposed.

To consider the particle stiffness, we employed a particle stiffness function f_r. The terms $\boldsymbol{\sigma}_{\text{col}}$, $\boldsymbol{q}^E_{col}$, and Γ_{col} are multiplied by this stiffness function. A function suggested by Hwang and Hutter (1995) is considered:

$$f_r = \left[1 + 2\frac{d}{s}\left(\frac{\rho_p T}{E_p}\right)^{1/2}\right]^{-1} \tag{12}$$

where E_p is Young's modulus of the particle; s is the mean separation distance among particles, as expressed in Eq.(13). Note that the particle stiffness function is equal to one while the E_p is infinite (rigid particle), i.e., no particle stiffness modification for the kinetic theory is taken. The value of f_r ranges from 0 to 1, reflecting varying degrees of particle stiffness.

$$s = \frac{\sqrt{2}}{12}\frac{d}{G(\Phi)} \tag{13}$$

To simplify the formulation in the original version by Feng et al. (2025), we employed a straightforward equation for the auxiliary function J in Appendix B, as developed by Vescovi et al. (2013):

$$J = \frac{1+\varepsilon_n}{2} + \frac{\pi}{32}\frac{[5+2(1+\varepsilon_n)](3\varepsilon_n - 1)G][5+4(1+\varepsilon_n)G]}{[24-6(1-\varepsilon_n)^2 - 5(1-\varepsilon_n)^2]G^2} \tag{14}$$

2.4. Unified model

To sum up, a unified elastoplasticity-based frictional-collisional phase transition model is developed by using Eq. (1). The critical-state-based elastoplastic model is employed to depict the strain rate-independent frictional stress, while the modified kinetic theory model is adopted to describe the strain rate-dependent collisional stress. Table 1 lists the basic input parameters in this unified phase transition model. Important input parameters for the frictional stress part include: dimensionless referential elastic modulus E_0, Poisson's ratio ν, and elastic constant controlling nonlinear stiffness n describing the elastic behavior; parameters e_{ref}, λ, and ξ for the evolution critical void ratio; coefficients A_d and k_p depicting the nonlinear plastic hardening characteristics; parameters n_p and n_d depicting the stress dilatancy and shear softening. Considering the importance of parameters in the frictional stress part, a brief calibration process is discussed. First, parameters e_{ref}, λ, and ξ can be determined via the critical state line (CSL) from the triaxial tests. In the CSL, the parameter e_{ref} is the reference void ratio where the mean effective frictional stress is zero; the parameter λ controls the slope of the CSL; the parameter ξ controls the position of the inflection point in the CSL. Second, Poisson's ratio ν can be obtained through data from triaxial tests by plotting the axial strain versus radial strain and determining ν from the slope of this line. Additionally, Poisson's ratio can also be determined from the literature, as suggested by Yin et al. (2020), ranges from 0.2 to 0.25. Parameters E_0 and n can be obtained from isotropic compression tests. The parameter n usually takes the value of 0.5–0.7, as suggested by Yin et al. (2020). Third, critical angle φ_c can take the value from the drained direct shear test or drained triaxial test. Parameter e_0 is the initial void ratio. Fourth, parameters A_d, k_p, n_p, and n_d can be derived from undrained or drained triaxial tests. As suggested by Yin et al. (2020), both n_p and n_d can take the value of 1 when direct determination of these parameters is challenging. Parameter A_d can take the value of 0.5–1.5, while k_p usually takes the value from 0.0001 to 0.01.

3. Model evaluation

This section presents the numerical implementation of the proposed elastoplasticity-based phase transition model. First, a description of the simple shear element test and the derivation of the granular temperature is provided. Next, the element simulation of the modified kinetic theory is discussed, considering key factors such as strain rate path and particle stiffness. Finally, the proposed phase transition model's effectiveness is demonstrated through element simulation, highlighting its capability to capture the phase transition behavior accurately.

3.1. Simple shear test

The numerical analysis of the constitutive model at the element level is crucial for its application in boundary value problems for practical engineering scenarios. Traditional laboratory element tests, such as the triaxial test commonly used in soil mechanics, are insufficient to capture fluid-like behavior at large strains. In contrast, the simple shear test can uniquely capture both solid-like behavior at small strains and fluid-like responses at large strains. Given the significance of undrained responses in describing the liquefaction phenomenon of granular media, the undrained simple shear test is employed in this study.

Fig. 1 shows the stress and strain condition in the simple shear test. The sample is subjected to a prescribed shear strain $\gamma = \partial u/\partial y$. Under the constant volume condition (i.e., undrained condition), the vertical strain remains zero, and only vertical stress (i.e., the hydrostatic stress p) and shear stress τ are generated. The hydrostatic and shear stresses of the frictional component can be expressed as p_f and τ_f, respectively. Following Eq. (2), the hydrostatic and shear stress of the collisional component can be written as $p_{col} = 4G(\Phi)F(\Phi,\varepsilon_n)\rho T$ and $\tau_{col} = \eta_v\dot{\gamma}$, respectively. Note that the $\dot{\boldsymbol{\varepsilon}}_{xy}$ in Eq. (2) is related to the shear strain rate $\dot{\gamma}$ in the simple shear test via $\dot{\boldsymbol{\varepsilon}}_{xy} = 0.5\dot{\gamma}$.

To obtain the frictional stress p_f and τ_f, an explicit numerical integration scheme can be employed. A detailed description of the integration process can be found in Yin et al. (2020). For calculating the collisional stresses (p_{col} and τ_{col}), the granular temperature T, governed by the energy balance equation (Eq. (9)), must first be derived. In the context of the steady simple shear test, the divergence of the energy flux

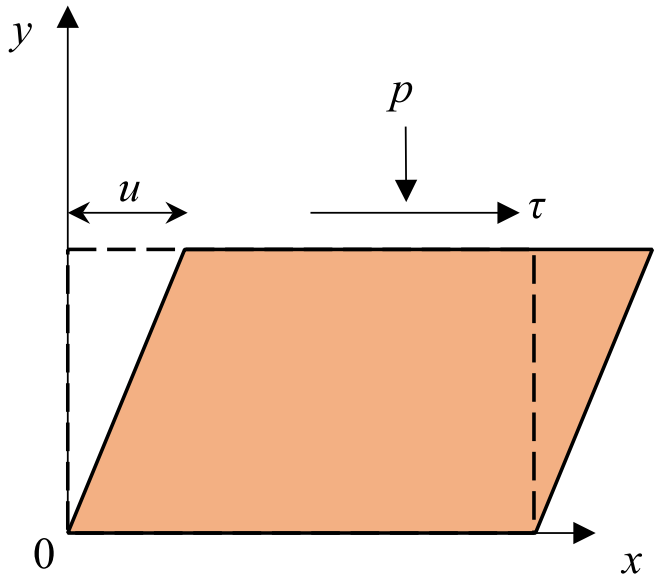

Fig. 1. Illustration scheme of the simple shear test.

is neglected, assuming that all energy generated by the work of the collisional shear stress is fully dissipated through the collisional mechanism. By substituting the collisional stress (p_{col} and τ_{col}) and the collisional dissipated energy Γ_{col} into the energy balance equation, we can derive the granular temperature T (see Eq. (15)). The collisional stress p_{col} and τ_{col} can also be determined using this granular temperature. In scenarios beyond element test conditions, such as in finite element analysis, the divergence of the energy flux becomes significant. In these cases, an explicit forward algorithm can be employed. This involves using the current granular temperature to calculate both the divergence of the energy flux and the collisional dissipated energy via Eqs. (10)–(11). Subsequently, the granular temperature is updated according to Eq. (9).

$$T = \frac{2d^2\dot{\gamma}^2}{15}\frac{J}{\left(\left(1-\varepsilon_n^2\right)\left(1+\frac{3}{32}c^*\right)\right)} \tag{15}$$

To evaluate the performance of the proposed phase transition model, three stress components are investigated: (i) the frictional stress at small strains, (ii) the collisional stress at large strains, and (iii) the unified frictional-collisional stress across the entire strain regime. This study examines the influence of three factors: particle stiffness, strain rate path, and concentration. Since particle stiffness and strain rate path are unrelated to frictional stress, and the effect of concentration on frictional stress was addressed in our previous study, the focus is on simulating (ii) the modified kinetic theory and (iii) the proposed phase transition model under these influencing factors. Detailed element simulations of the frictional stress are provided by Feng et al. (2025).

3.2. Simulation using modified kinetic theory

The effect of concentration, particle stiffness, and strain rate path on the performance of modified kinetic theory is first investigated. The basic input parameters are listed in Table 2, where different particle stiffness values of 1 kPa, 10 kPa, 1 MPa, and 10 MPa and different concentration values of 0.62, 0.60, 0.50, 0.40, 0.30, and 0.20 are considered. To investigate the influence of the strain rate path on collisional stress, different strain rate paths depicting the evolution of strain rate acceleration are employed, as shown in Figs. 2-4, where γ, $\dot{\gamma}$, and $\ddot{\gamma}$ represent the shear strain, strain rate, and strain acceleration, respectively. Herein a forward Eulerian explicit integration algorithm is employed. A small-time step $dt = 10^{-6}$ s is employed.

3.2.1. Influence of concentration

We first investigate the influence of concentration in this study. Different particle concentration values of 0.62, 0.60, 0.50, 0.40, 0.30, and 0.20 are considered with strain rate path 3. Fig. 5 presents the simulation results. The results show that specimens with higher concentrations can generate higher collisional stresses. It is observed that during shear rates from 0 to approximately 20 s^{-1}, the collisional stress remains near zero. However, beyond the shear rate of approximately 20 s^{-1}, the collisional stress becomes comparatively large, indicating that collisional stress is minimal when the material is solid-like. At a shear rate of 200 s^{-1}, samples with concentrations of 0.20, 0.30, and 0.40 exhibit vertical and shear stresses not exceeding 50 Pa. In contrast, the sample with a concentration of 0.50 shows stress more than twice that of the 0.40 concentration. The stress for the sample with a concentration of 0.60 is more than double that of the 0.50 concentration, approaching the concentration of 0.62. This suggests a strong nonlinear relationship between concentration and collisional stress. Specifically, as the concentration approaches the maximum volume fraction Φ_s, the collisional stress becomes infinite, whereas as the concentration approaches zero, the collisional stress approaches zero. This nonlinear relationship is attributed to spatial non-uniformities governed by concentration, as described by the radial distribution function in the modified kinetic theory. These findings suggest that the modified kinetic theory model can effectively consider the concentration-dependence characteristic.

Table 2
Material parameters in the collisional stress model.

ρ_p (kg/m^3)	d (m)	Φ_s	Φ_m	ε_r	E_p (kPa)	Concentration Φ
1000	1•10^{-3}	0.65	0.4	0.6	1, 10, 10^3, 10^4	0.20, 0.30, 0.40, 0.50, 0.60, 0.62

3.2.2. Influence of particle stiffness

This study also examines the ability of the modified kinetic theory model to describe particle stiffness-dependent characteristics. Different particle stiffness values of 1 kPa, 10 kPa, 1 MPa, and 10 MPa are considered with strain rate path 3. Fig. 6 presents the simulation results of the undrained simple shear test using the pure collisional stress model under varying particle stiffnesses. The results show that specimens with higher stiffness exhibit larger collisional stress. This suggests that the modified kinetic theory model can effectively capture the particle stiffness-dependent characteristics. In contrast, the model presented by Feng et al. (2025), which assumes rigid particles, tends to overestimate the collisional stress during granular flow. The sample's stiffness varies from 1 kPa to 10 kPa and 1 MPa, increasing by factors of approximately 10 and 100, respectively. Despite this significant increase in stiffness, both vertical and shear stress increase by approximately two times. This observation also indicates a strong nonlinear relationship between particle stiffness and collisional stress. Specifically, the collisional stress reaches an ultimate value as particle stiffness becomes infinite, whereas it approaches zero when particle stiffness approaches zero.

3.2.3. Influence of strain rate path

This study also investigates the modified kinetic theory stress using different strain rate paths. Fig. 7 illustrates the evolution of collisional hydrostatic stress, collisional shear stress, and granular temperature under different strain rate paths. These results indicate that the modified kinetic theory is sensitive to the strain rate path and, therefore, can capture the dependence on strain acceleration (see Fig. 7(c)–(d)).

Fig. 7(a) demonstrates a constant shear-to-vertical stress ratio, indicating a stable friction coefficient of the collisional stress. However, this value for granular flow must account for the contribution of frictional stress. While collisional stress exhibits a constant friction coefficient, this does not extend to granular media overall, with detailed discussion in Section 5.1. Fig. 7(b) demonstrates that as the strain rate increases from small to large values, the granular media transitions from a solid-like to a fluid-like state. In this transition, collisional stress is negligible in the solid-like state and becomes dominant in the fluid-like state. Notably, Fig. 7(b) shows that all specimens exhibit the same strain rate-stress relationship because the time effect is neglected in this figure. In contrast, Fig. 7(c) highlights the time effect, demonstrating that strain acceleration is effectively captured by the kinetic theory.

Fig. 7(d) further describes the evolution of granular temperature. In Path-1, the strain acceleration changes from positive to zero and then to a negative value. Consequently, the strain rate first increases, remains constant, and then decreases. Correspondingly, the granular temperature initially rises, then remains constant, and finally decreases, aligning well with the evolution of the strain rate. In Path-2, the strain acceleration varies from positive to negative and then back to positive. The strain rate increases, decreases, and then rises again, with the granular temperature following the same trend. In Path-3, there is constant strain acceleration and an increasing strain rate, resulting in a rise in granular temperature. These results under different strain rate paths demonstrate that the state variable, granular temperature, in the modified kinetic theory can accurately describe the dependence on the strain rate. It is important to note that Eq. (15) describes a positive correlation between T and $\dot{\gamma}^2$, which is consistent with experimental findings by Bagnold

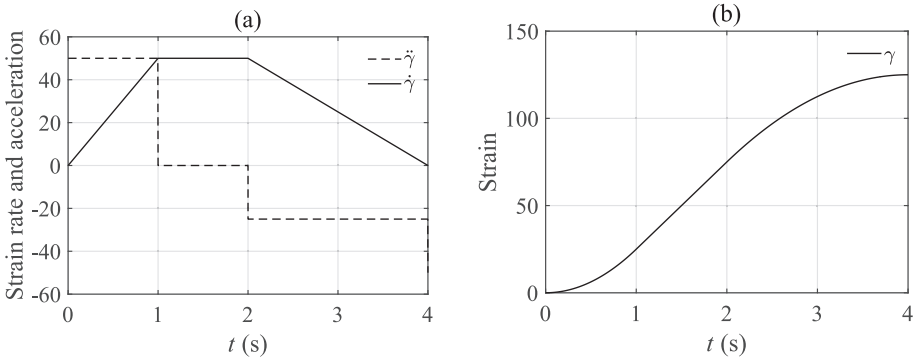

Fig. 2. Strain rate path-1: (a) Varying strain rate; (b) Varying strain.

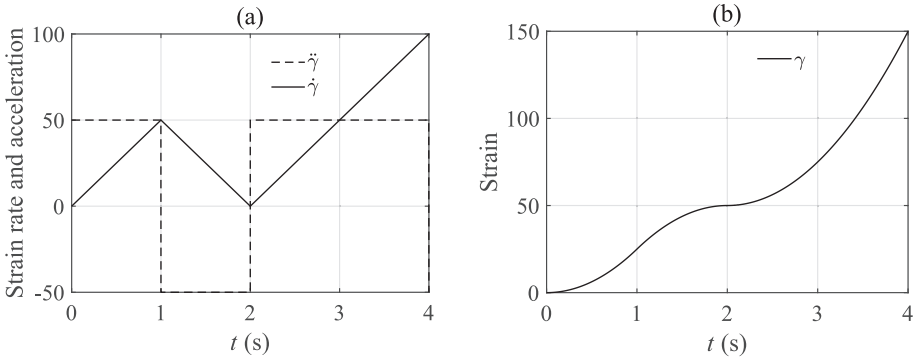

Fig. 3. Strain rate path-2: (a) Varying strain rate; (b) Varying strain.

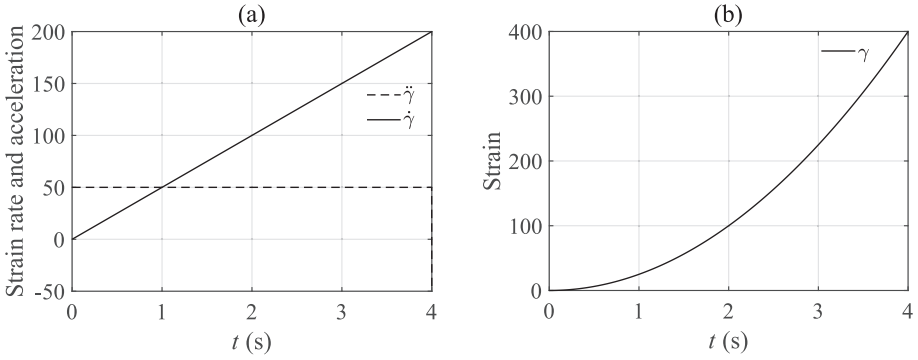

Fig. 4. Strain rate path-3: (a) Varying strain rate; (b) Varying strain.

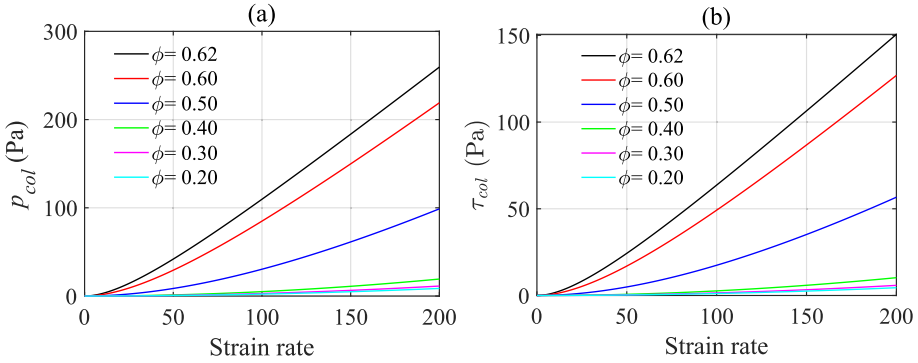

Fig. 5. Simulation of modified kinetic theory under different concentrations: (a) The evolution of vertical stress; (b) The evolution of shear stress ($E_p = 1$ MPa, strain rate path-3).

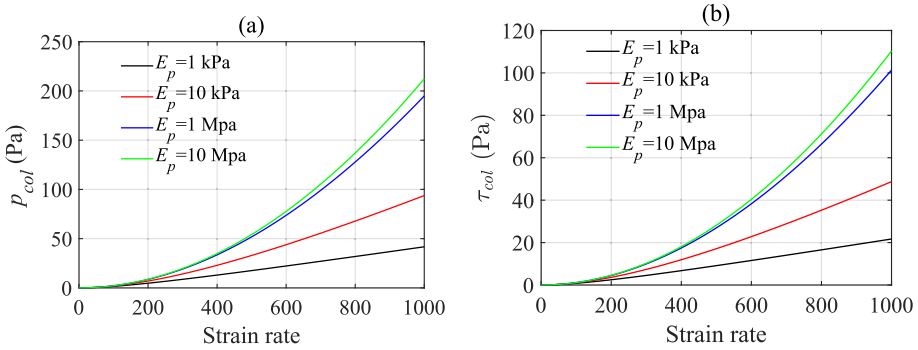

Fig. 6. Simulation of modified kinetic theory under different particle stiffnesses: (a) The evolution of vertical stress; (b) The evolution of shear stress ($\Phi = 0.2$, strain rate path-3).

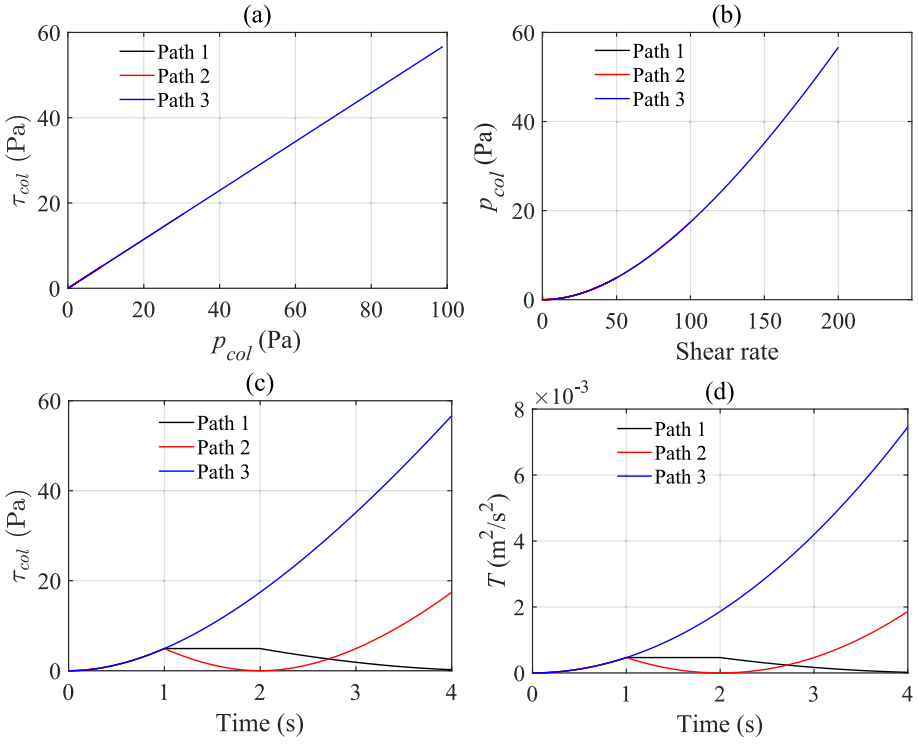

Fig. 7. Simulation of modified kinetic theory under different strain rate paths: (a) The relation between vertical stress and shear stress; (b) The evolution of vertical stress; (c) The evolution of shear stress; (d) The evolution of granular temperature ($E_p = 1$ MPa, $\Phi = 0.5$).

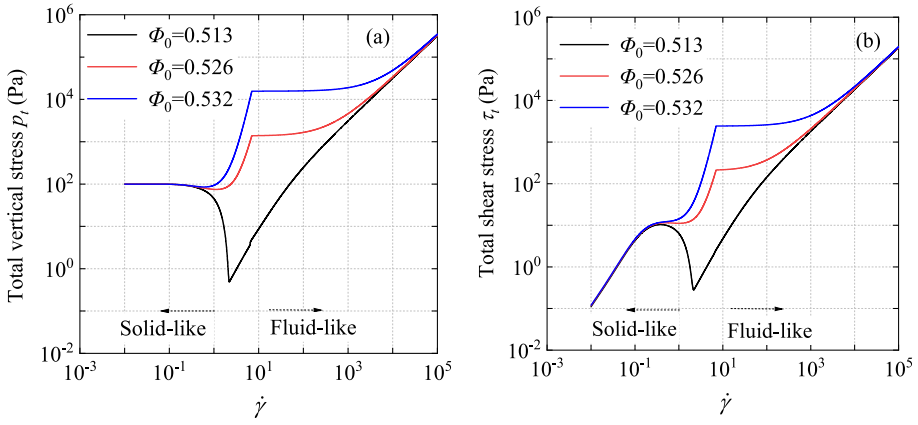

Fig. 8. Simulation of proposed elastoplasticity-based phase transition model under different initial concentrations: (a) The evolution of total vertical stress; (b) The evolution of total shear stress.

(1954). This consistency demonstrates the effectiveness of the modified kinetic theory in depicting fluid-like stress.

3.3. Simulation using proposed elastoplasticity-based phase transition model

3.3.1. Influence of concentration

We further simulate the undrained simple shear test using the proposed elastoplasticity-based phase transition model. The basic parameters for the proposed phase transition model are provided in Table 1. Different initial concentrations ($\Phi_0 = 0.513, 0.526, 0.532$) are considered to examine the effect of the initial state on granular behavior during large deformation flow. A small time step ($dt = 10^{-6}$ s) is used, with a total simulation time of 100 s. The initial hydrostatic stress p_t is set to 100 Pa. To accurately simulate frictional stress and expedite the simulation of collisional stress, the simulation begins with a zero shear rate and strain acceleration of 10 s^{-2} for the first 2 s, followed by a strain rate acceleration of 1000 s^{-2} applied from 2 to 100 s.

Fig. 8 illustrates the evolution of vertical and shear stress for different initial concentrations. It is evident that the initial concentration significantly influences the granular flow responses, particularly at the small strain rate regime. However, the total stress including vertical stress and the shear stress for different initial concentrations tend to converge at the large strain rate regime. This suggests that the initial state of the granular media has minimal influence on the high strain rate regime. Fig. 8 also indicates that the shear rate range approximately from 10^0 to 10^1 represents the solid–fluid transition range for these simulations, characterized by constant frictional stress and attainment of a critical state. Notably, this transition range may vary across materials.

To explain the observation in Fig. 8, the hydrostatic and shear components from total, frictional, and collisional stresses of both dense and loose samples are derived. Fig. 9 illustrates these results of the loose specimen ($\Phi_0 = 0.513$). At the small strain rate regime (e.g., $\dot{\gamma}$ ranges from 0 to 10^1), the frictional stress is dominant, indicating the frictional stress dominates in the solid-like state. At the large strain rate regime (e.g., $\dot{\gamma}$ higher than 10^1), the collisional stress is dominant, indicating the collisional stress dominates in the fluid-like state. This indicates that the proposed model effectively satisfies the requirement of describing the solid-like and fluid-like behaviors of granular flows. Additionally, the critical-state-based elastoplastic stress model accurately captures the evolution of frictional stress in loose samples. Specifically, it exhibits shear softening and achieves a relatively small residual strength at the critical state, which is indicative of the liquefaction phenomenon.

Fig. 10 further illustrates the hydrostatic and shear components from total, frictional, and collisional stresses of the dense specimen ($\Phi_0 = 0.532$). The results in Fig. 10 match well with observations in Fig. 9, reinforcing that frictional stress dominates in the solid-like state, while collisional stress governs the fluid-like state. Fig. 10 also indicates that the dense specimens exhibit shear hardening and ultimately reach the critical state line, achieving a constant residual strength value. In contrast to Fig. 9, the critical state strength of the dense sample remains significantly constant, whereas this strength of the loose sample approaches zero. This large critical state strength results in a flat stage of the total stress in Fig. 10, indicating that this stage remains solid-like due to the smaller collisional stress.

3.3.2. Influence of particle stiffness

We further investigate the influence of particle stiffness in this study. Different particle stiffness values of 1 kPa, 10 kPa, 1 MPa, and 10 MPa are employed with the initial concentration of 0.513. Fig. 11 presents the simulation results, showing that specimens with higher stiffness generate greater stresses. This demonstrates that the developed elastoplasticity-based phase transition model effectively accounts for stiffness-dependent characteristics through the collisional stress component. Fig. 11 once again suggests that the enhanced solid–fluid phase transition model can effectively capture the particle stiffness-dependent characteristics. In contrast, the model presented by Feng et al. (2025), which assumes rigid particles, tends to overestimate the granular stress.

3.3.3. Influence of strain rate path

We further examine the influence of strain rate paths on the unified phase transition model using the strain rate paths shown in Figs. 2–4. To reduce computational cost, the total simulation time is set to 4 s. A loose sample with an initial concentration of 0.513 is employed. The simulation results, presented in Fig. 12, reveal that under different strain rate paths, the loose sample rapidly reaches the critical state at the liquefaction point, i.e., the solid-like frictional stress diminishes rapidly. Subsequently, the samples exhibit varying fluid-like behaviors depending on the strain rate paths. These results demonstrate that the developed elastoplasticity-based phase transition model effectively captures strain acceleration-dependent characteristics through the collisional stress component.

In our proposed model, the total stress is composed of two components: frictional stress and collisional stress. The frictional stress reaches a critical state within a limited strain, typically less than 0.5, indicating that strain has a limited influence on frictional stress. In contrast, collisional stress is rate-dependent, meaning that it is significantly influenced by the strain rate and is calculated based on the strain rate rather than strain. In other words, both the collisional stress and strain are outcomes of the strain rate, and collisional stress is not directly related to strain. Therefore, strain primarily influences the proposed model through its effect on the frictional component. Given this, we can

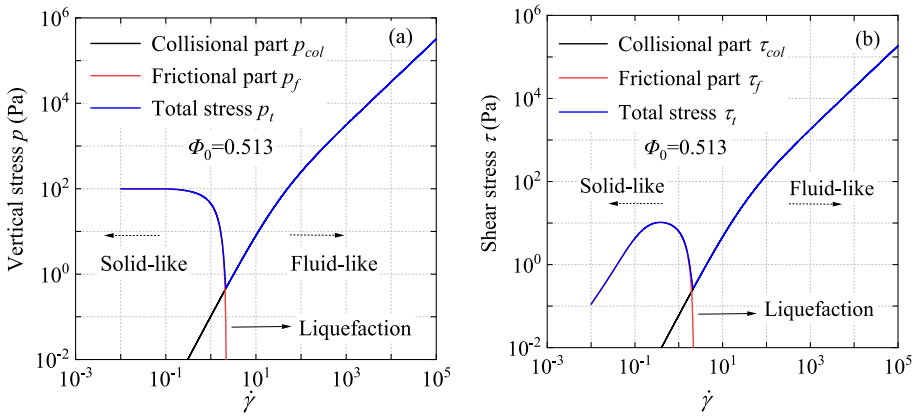

Fig. 9. The evolution of the collisional, frictional, and total stress for the initial loose sample ($\Phi_0 = 0.513$): (a) The evolution of vertical stress; (b) The evolution of shear stress.

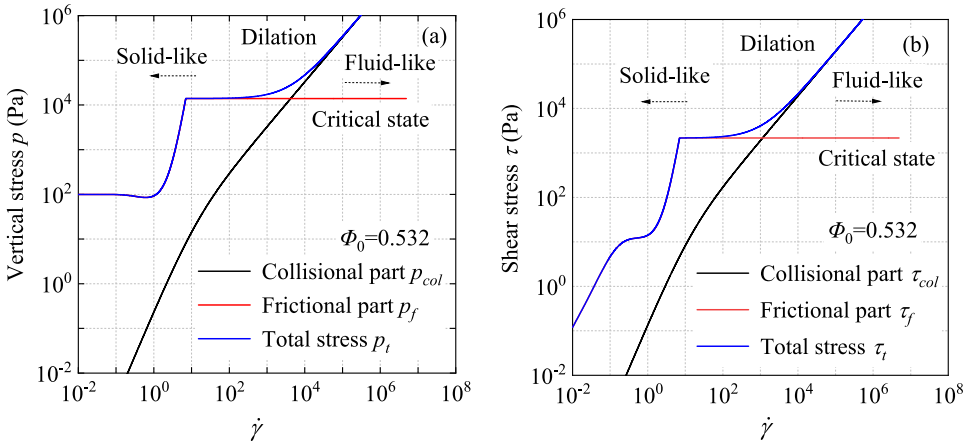

Fig. 10. The evolution of the collisional, frictional, and total stress for the initial dense sample ($\Phi_0 = 0.532$): (a) The evolution of vertical stress; (b) The evolution of shear stress.

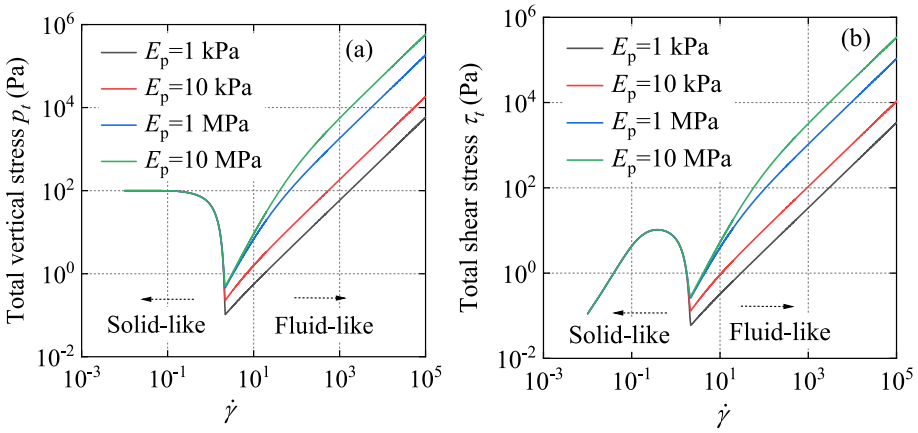

Fig. 11. The evolution of total stress under different particle stiffnesses: (a) The evolution of vertical stress; (b) The evolution of shear stress ($\Phi_0 = 0.513$).

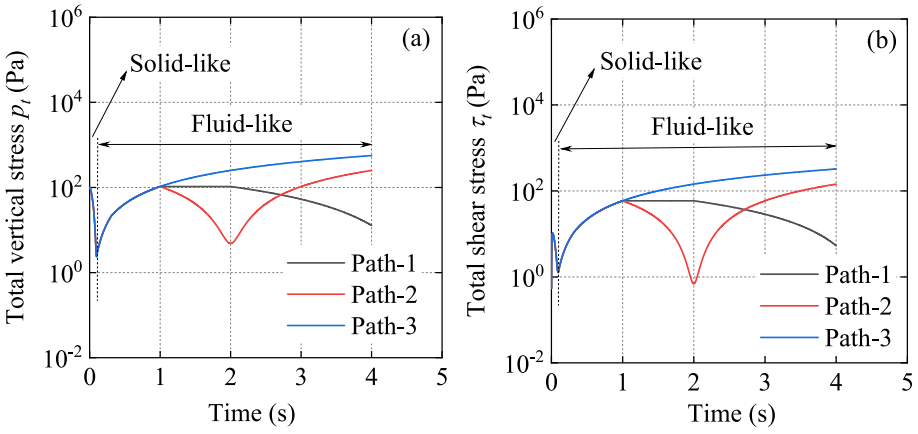

Fig. 12. The evolution of total stress under different strain rate paths: (a) The evolution of vertical stress; (c) The evolution of shear stress ($\Phi_0 = 0.513$).

conclude that strain has a minimal impact on the proposed model.

4. Simulating experimental data

The critical-state-based elastoplastic framework for frictional stress has been extensively validated in prior studies (Yin et al., 2020). To maintain conciseness and avoid redundancy, we omitted a detailed revalidation of the frictional stress model in this work. Only the performance of the proposed elastoplasticity-based phase transition model is evaluated against experiment results by Savage and Sayed (1984) in this section.

4.1. Polystyrene beads

Savage and Sayed (1984) employed annular shear tests to investigate the response of granular materials (e.g., polystyrene and glass beads)

under constant volume conditions, enabling the use of undrained simple shear tests. The basic numerical setup follows Feng et al. (2025), and the parameters for polystyrene beads are listed in Table 1. The initial pressure is set to 500 Pa, and four initial concentrations ($\Phi_0 = 0.526$, 0.463, 0.444, and 0.408) are considered. Using the proposed phase transition model, Figs. 13 and 14 illustrate the normalized vertical stress-shear rate and normalized shear stress-shear rate relationships on a logarithmic scale. The results show that the proposed elastoplasticity-based phase transition model accurately approximates experimental responses. During the transition from a solid-like to a fluid-like state, the total vertical and shear stresses initially decrease at low strain rates and subsequently increase at high strain rates, with the dominant stress shifting from frictional to collisional. This validation highlights the effectiveness of the proposed elastoplasticity-based model.

4.2. Glass beads

To further validate the applicability of the proposed phase transition model in capturing the behavior of granular flow, element tests using glass beads were conducted. The basic parameters for the glass beads are listed in Table 1, and the loading conditions are identical to those in subsection 4.1. Four initial concentrations were considered ($\Phi_0 = 0.521$, 0.490, 0.467, and 0.450). Figs. 15 and 16 illustrate the normalized vertical stress-shear rate and normalized shear stress-shear rate relationships for the glass beads, respectively. The results highlight the proposed model can reasonably approximate experimental responses observed in laboratory tests. Moreover, the model effectively captures the stress evolution of granular flow during the transition from a solid-like to a fluid-like state.

5. Comparative analysis

The previous section evaluated the proposed elastoplasticity-based phase transition model. This section compares the simulation results of the proposed unified phase transition model with two existing granular flow models: the $\mu(I)$ rheology model and the state-equation-based phase transition model by Vescovi et al. (2013). These models were selected for comparison for the following reasons: (i) This study does not aim to compare advanced models (e.g., Guo et al., 2021; Marveggio et al., 2022; Wang and Wu, 2024), as their differences are already well established. Instead, the focus is to elucidate the different treatments of frictional and collisional stress. (ii) For the frictional stress component, the proposed model incorporates the critical state theory in a manner consistent with most advanced models, except for the approach by Vescovi et al. (2013). (iii) For the collisional stress component, the proposed model employs kinetic theory, unlike the phenomenological rheology approach used in the $\mu(I)$ model.

This study, therefore, focuses on numerical comparisons with the $\mu(I)$ and Vescovi et al. (2013) models to highlight the unique contributions of the proposed approach. The first comparison addresses collisional stress, while the second emphasizes the distinct implementations of frictional stress.

5.1. Comparison with $\mu(I)$ rheology model

5.1.1. $\mu(I)$ rheology model

The $\mu(I)$ rheology model, as the name suggests, employs two non-dimensional quantities, i.e., friction coefficient μ and inertial number I, to describe the phenomenological rheology of granular flow. These parameters were developed by the French research group GDR-MiDi (2004). Under the simple shear test, the friction coefficient μ, defined as a ratio between total hydrostatic and shear stress, as follows:

$$\mu = \frac{\tau_t}{p_t} \tag{16}$$

The inertial number I is expressed via Eq. (17). It can be seen as a ratio between the microscopic time scale $2d/\sqrt{p_t/\rho_s}$, associated with the transversal motion of a particle under the normal stress p_t, and the macroscopic time scale, $1/|\dot{\gamma}|$, associated with the shear motion.

$$I = \frac{2d|\dot{\gamma}|}{\sqrt{p_t/\rho_s}} \tag{17}$$

Based on the experimental results, Jop et al. (2006) has proposed the following relation to depict the relation between μ and I during granular flow:

$$\mu(I) = \mu_s + \frac{\mu_d - \mu_s}{I_0 + I} I \tag{18}$$

where μ_s and μ_d are the static and dynamic friction coefficients, respectively.

5.1.2. Comparative discussion

To compare the proposed elastoplasticity-based phase transition model with the μ-I model by Jop et al. (2006), we derive the relation between friction coefficient μ and inertial number I from the results in subsection 3.3. The results are shown in Fig. 17, indicating that the evolution of the friction coefficient μ, using the proposed phase transition model, has three distinct stages:

5) Small strain rate regime (i.e., inertial number I ranges from 0 to 10^{-2}): The friction coefficient μ increases to a constant value at point A. At this stage, the granular media is mainly controlled by the frictional stress in the solid-like state. As the frictional stress moves from the initial

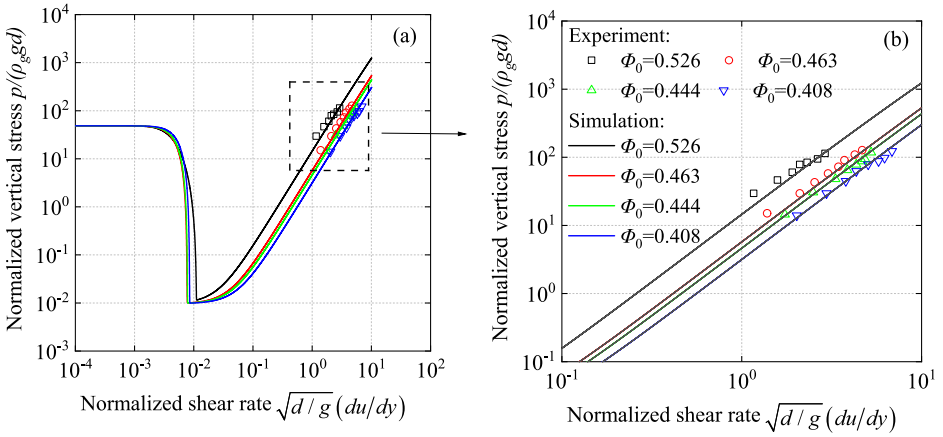

Fig. 13. Comparison of the vertical stress from numerical and experimental results for polystyrene beads: (a) A wide range of shear rate from 10^{-4} to 10^{2}; (b) A small range of shear rate from 0.1 to 10.

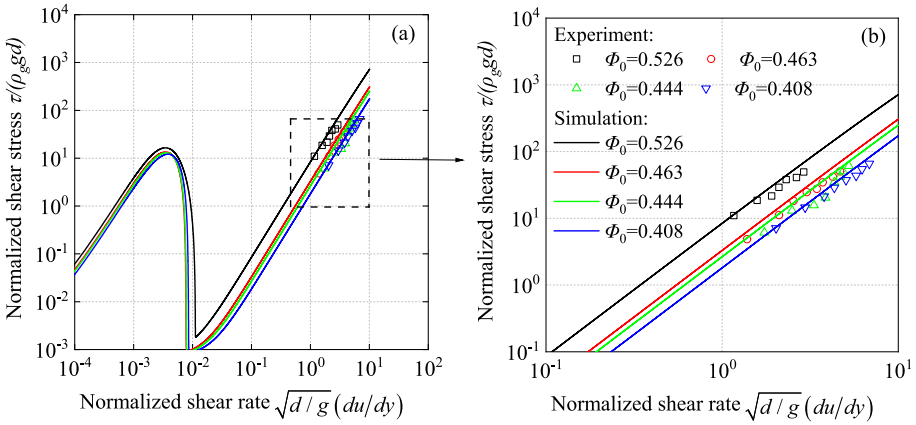

Fig. 14. Comparison of the shear stress from numerical and experimental results for polystyrene beads: (a) A wide range of shear rate from 10^{-4} to 10^{2}; (b) A small range of shear rate from 0.1 to 10.

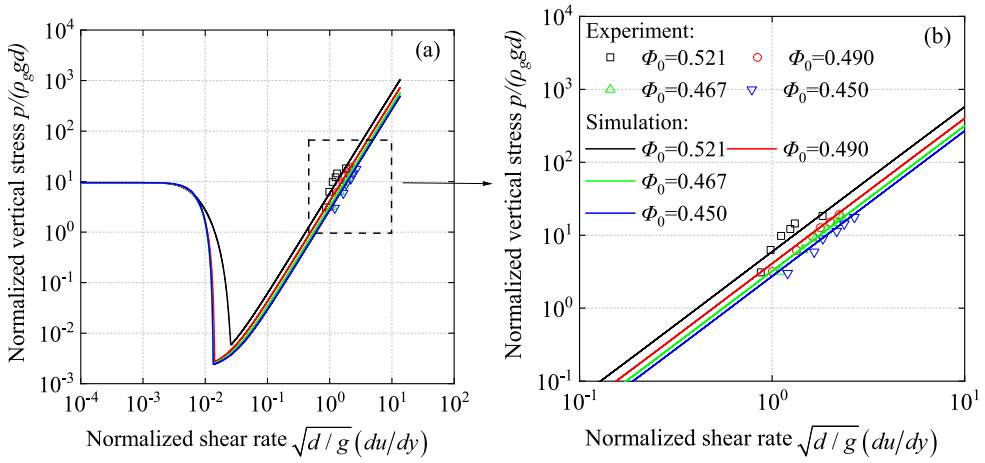

Fig. 15. Comparison of the vertical stress from numerical and experimental results for polystyrene beads: (a) A wide range of shear rate from 10^{-4} to 10^{2}; (b) A small range of shear rate from 0.1 to 10.

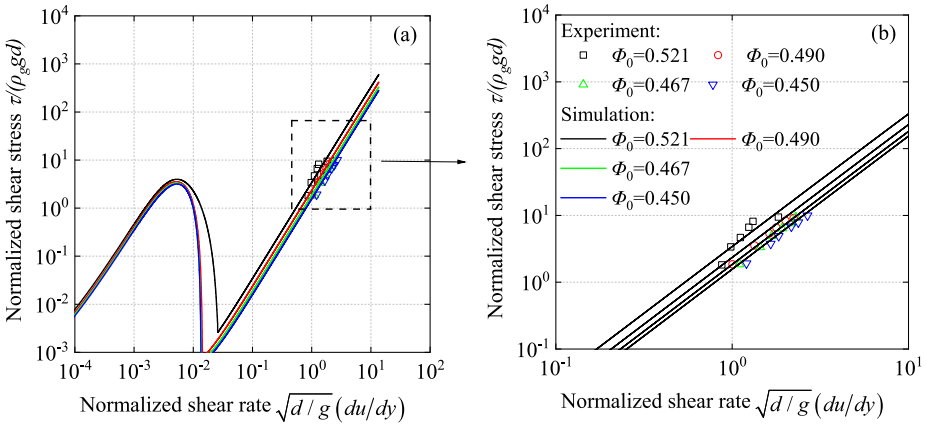

Fig. 16. Comparison of the shear stress from numerical and experimental results for polystyrene beads: (a) A wide range of shear rate from 10^{-4} to 10^{2}; (b) A small range of shear rate from 0.1 to 10.

state to the critical state, the friction coefficient μ rises from nearly zero to point A, which can be described as the critical-state point. It should be emphasized that granular flow initiates at the critical state, marking the transition from a solid-like to a fluid-like state, where the material deforms indefinitely without significant changes in stress or volume.

6) Large strain rate regime (i.e., inertial number I ranges from 10^{-2} to 10^{1}): The friction coefficient μ increases from the critical-state point A to point B. At this stage, the granular media is mainly controlled by the frictional stress and the collisional stress. As the collisional stress rises with the increasing strain rate and the frictional stress maintains the residual strength, the friction coefficient μ rises from the critical state to the constant value.

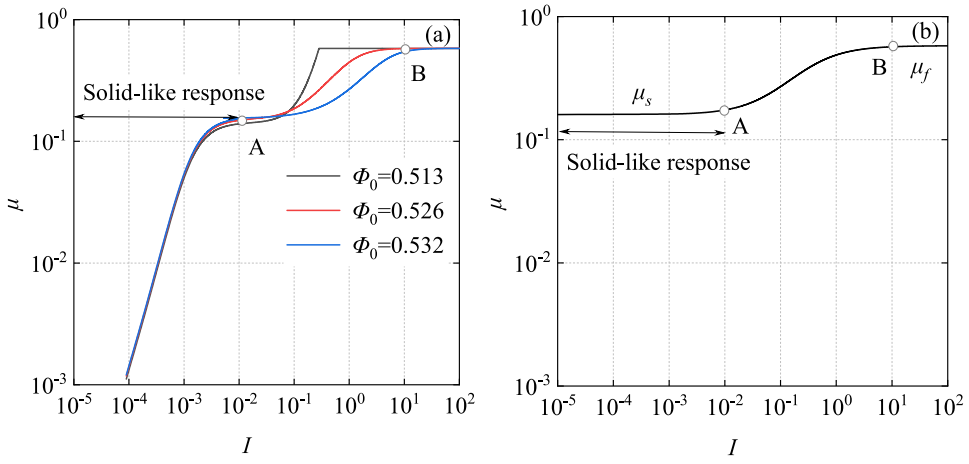

Fig. 17. The relation between the friction coefficient μ and the inertial number I (a): Proposed phase transition model with different initial concentrations; (b) μ-I model by Jop et al. (2006) ($\mu_s = 0.16$, $\mu_d = 0.58$).

7) Very large strain rate regime (i.e., inertial number I larger than 10^1): The friction coefficient μ remains the constant value of point B. At this stage, the granular media is mainly controlled by the collisional stress and the frictional stress is insignificant. The friction coefficient of the proposed model is the ratio between the collisional shear and collisional hydrostatic stress, which is constant, as evidenced in Fig. 7 (a).

Fig. 17(b) presents the results from the μ(I) model by Jop et al. (2006), where the friction coefficient μ rises from the static friction coefficient μ_s to the dynamic friction coefficient μ_d. By comparing to Fig. 17 (a), we can obtain: (i) The μ(I) model captures only the latter two stages observed in Fig. 17(a). Hence the μ(I) model can only be seen as a purely fluid-like model, rather than the solid–fluid phase transition model. On the other hand, the proposed phase transition model not only replicates the rheology of granular media after the initiation of flow but also accurately depicts the behavior before flow initiation. (ii) The proposed phase transition model can effectively reflect the effect of concentration, which the μ(I) model cannot. (iii) The static friction coefficient μ_s in the μ(I) model may be equal to this coefficient at the critical state of the proposed model, while the dynamic friction coefficient μ_d may be equal to the ratio between the collisional shear and collisional hydrostatic stress of the proposed model.

5.2. Comparison with state-equation-based phase transition model

5.2.1. State-equation-based phase transition model (SEPTM)

Within the unified frictional-collisional solid–fluid phase transition framework, the widely employed phase transition model integrates a different frictional stress model with the collisional stress model using the same kinetic theory discussed in subsection 3.2 (e.g., Johnson and Jackson, 1987Johnson et al., 1990; Berzi et al., 2011; Vescovi et al., 2013). This frictional stress component usually employs the Mohr-Coulomb criterion to relate the hydrostatic stress with the shear stress and adopts the equation of state with critical state idea to describe the hydrostatic stress. Given this, we name this kind of unified solid–fluid phase transition model as the state-equation-based phase transition model (SEPTM), while employing EPPTM to replace the proposed elastoplasticity-based phase transition model for clarity.

Herein one typical form of the frictional stress component in the SEPTM presented by Vescovi et al. (2013) is given. Under under simple shear test, the hydrostatic and shear stress in the Mohr-Coulomb criterion is given as:

$$\tau_f = \tan\varphi_s p_f \tag{19}$$

where φ_s is the frictional angle.

The hydrostatic stress is expressed using the equation of state, as follows:

$$p_f = f_0 \frac{K_p}{d} \tag{20}$$

where K_p is the particle stiffness, related to the elastic modulus via the $K_p = \pi d E_p/8$; f_0 is a function of the concentration, expressed as follows:

$$f_0 = \begin{cases} a\dfrac{\Phi - \Phi_{rlp}}{(\Phi_s - \Phi)} \left(\Phi > \Phi_{rlp} \text{ and } \Phi_{rlp} < \Phi_s\right) \\ 0 \end{cases} \tag{21}$$

where a is a parameter; Φ_{rlp} is the minimum concentration at which a disordered packing exists. While the concentration is smaller than this concentration, the frictional stress disappears.

We first simulate the undrained simple shear test using the state-question-based phase transition model with different concentrations. The basic parameters for the state-question-based phase transition model are provided in Table 3. The same concentrations ($\Phi_0 = 0.513$, 0.526, 0.532) are considered. The simulation set is the same as in the subsection. 3.3. The total stress is calculated via Eq. (1), the frictional stress employs the equation of state (i.e., Eqs. (19)–(21)) while the collisional stress adopted the modified kinetic theory in subsection 2.3.

Fig. 18 shows the evolution of total hydrostatic and shear stress for different concentrations using the SEPTM. Total hydrostatic and shear stress differs under the different concentrations. However, all of the total stresses for different concentrations tend to converge at the large strain rate regime. This observation matches well with Fig. 8, suggesting that the initial state of the granular media has minimal influence on the high strain rate regime. For different concentrations, the frictional stress

Table 3
Input parameters in the state-equation-based phase transition model.

	Symbol	Parameter	Value
σ_{col}	ρ_p	Particle density (kg/m^2)	2000
	d	Diameter (m)	$1\bullet10^{-3}$
	ϕ_s	Void ratio parameter	0.55
	ϕ_m	Volume fraction parameter	0.4
	ε_r	Effective restitution coefficient	0.6
	E_p	Particle's Young's modulus (Pa)	$3\bullet10^6$
σ_f	a	Dimensionless referential coefficient	$2.8\bullet10^{-3}$
	Φ_{rlp}	Random loose packing concentration	0.520
	p_{at}	Atmospheric pressure (kPa)	101.3
	K	Particle stiffness	0
	φ_s	Frictional angle	9.09
	d	Diameter (m)	$1\bullet10^{-3}$

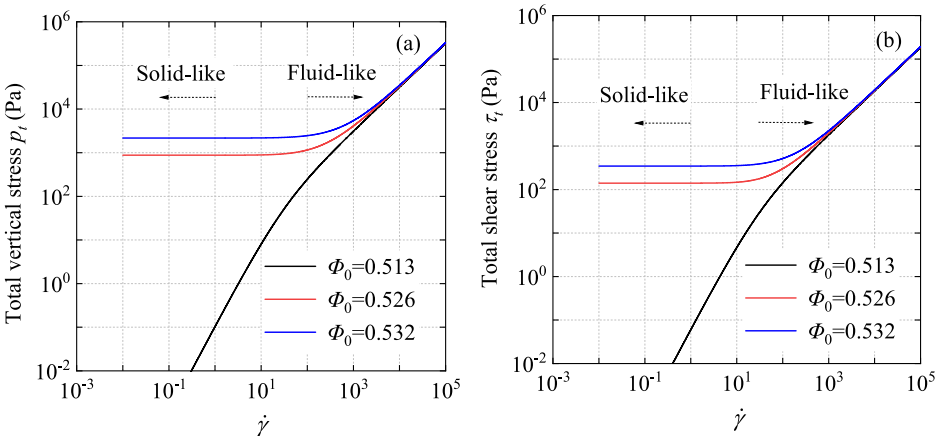

Fig. 18. Simulation results using SEPTM with different initial concentrations: (a) The evolution of vertical stress; (b) The evolution of shear stress.

dominates in the solid-like state, while collisional stress governs the fluid-like state, which indicating this model can also effectively describe the phase transition from solid-like to fluid-like.

5.2.2. *Comparative discussion*

To further analyze the frictional-collisional phase transition model, we compare the results of the loose sample using the EPPTM and SEPTM, which can be seen in Fig. 19. The difference between EPPTM and SEPTM lies in the solid-like state, which is governed by the frictional stress. The EPPTM can describe the evolution from the initial state to the critical state, corresponding to the liquefaction point, while the SEPTM directly equals the frictional stress as zero. Fig. 20 also compares the evolution of results for the dense sample using the EPPTM and SEPTM. Similar to Fig. 19, the difference between these two models lies in the solid-like state. The EPPTM can describe the evolution from the initial state to the critical state, where the dense sample behaves as shear dilatancy and obtains a residual strength at the critical state. The SEPTM directly describes the frictional stress as a constant strength at the critical state.

According to these observations, we can conclude that both the EPPTM and SEPTM can describe the solid–fluid phase transition phenomenon and consider the effect of concentration, but the difference lies in describing solid-like behavior using a distinct implementation of critical state theory. SEPTM only describes the frictional stress at the critical state as the solid-like behavior and the proposed elastoplasticity-based phase transition model describes the frictional stress from the initial state to the critical state. Furthermore, the concentration of the SEPTM is the critical-state concentration rather the initial concentration.

Fig. 21 further presents the relation between friction coefficient μ and inertial number I using the SEPTM. It is clear that the sample with larger initial concentrations (i.e., $\Phi_0 = 0.526, 0.532$) has a similar tendency shown in the μ-I model, both the SEPTM and μ-I model can accurately depict the fluid-like state. The sample with a smaller initial concentration ($\Phi_0 = 0.513$) has a constant μ value. This behavior can be explained by considering the two components of the stress. When the concentration is low, the frictional stress becomes negligible, as indicated by Eq. (21). Consequently, the friction coefficient μ depends solely on the collisional stress, which remains constant, as discussed in subsection 3.2.3. This observation indicates that the SEPTM can more effectively reflect the effect of the concentration than the μ(I) model.

5.3. *Summary*

Based on the comparative analysis above, the differences between the proposed elastoplasticity-based phase transition model (EPPTM), the state-equation-based phase transition model (SEPTM), and the μ(I) model are summarized in Table 4. The proposed EPPTM can be regarded as a full-range phase transition model, capable of describing the stress evolution from the initial state to the critical state and further to the fluid-like state. It is also concentration-dependent. The SEPTM can be regarded as a partial-range phase transition model, which describes the stress at the critical state to the fluid-like state without considering the process from the initial state to the critical state. It also considers the concentration-dependent characteristics. The μ(I) model can be regarded as a purely fluid-like model, only describing the stress at the fluid-like state. It captures the rheological behavior in a simple form but

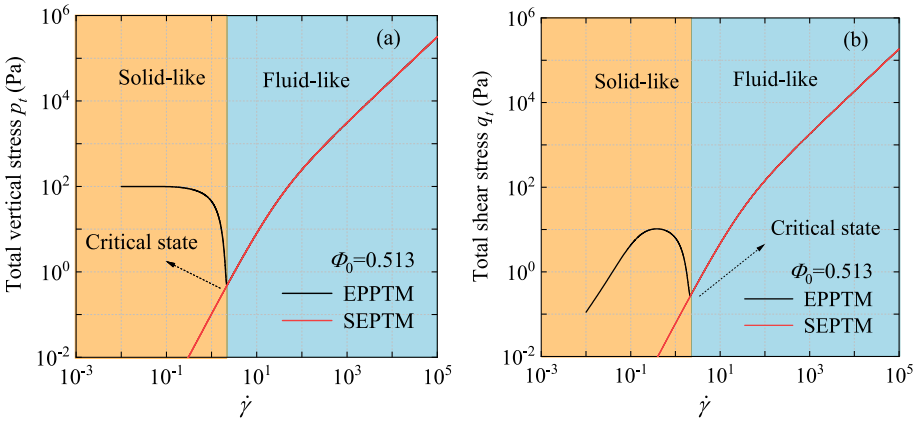

Fig. 19. Comparison of undrained simple shear simulation results using EPPTM and SEPTM with loose sample: (a) The evolution of vertical stress; (b) The evolution of shear stress.

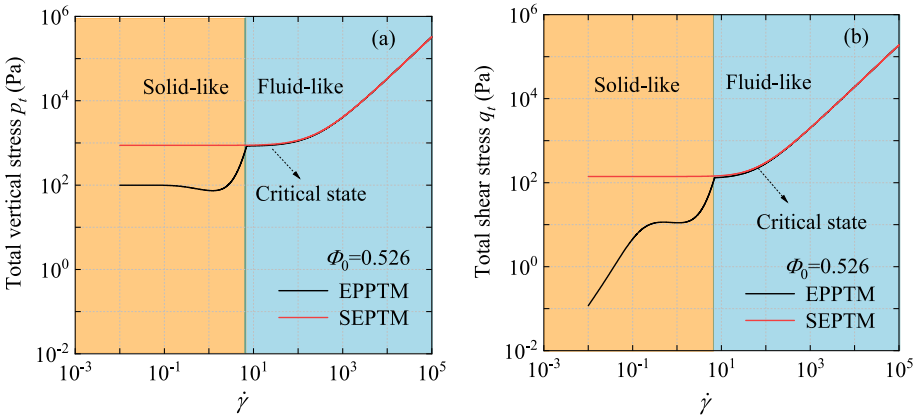

Fig. 20. Comparison of undrained simple shear simulation results using EPPTM and SEPTM with dense sample: (a) The evolution of vertical stress; (b) The evolution of shear stress.

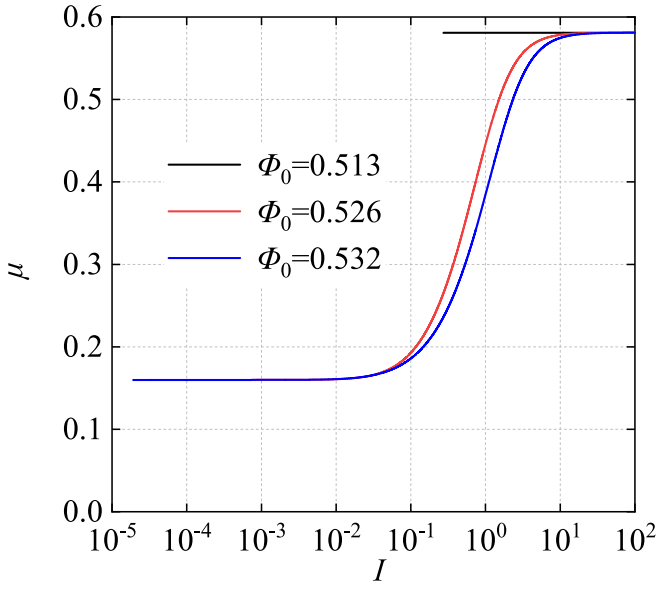

Fig. 21. The relation between the friction coefficient μ and the inertial number I using SEPTM with different initial concentrations.

does not consider concentration-dependent characteristics.

Despite the above differences, the number of parameters in these models is noteworthy (see Table. 4). The elastoplasticity-based phase transition model, state-equation-based model, and μ(I) model require 18, 12, and 5 parameters, respectively. While the elastoplasticity-based model captures full-range phase transitions, it demands the most parameters. The state-equation-based model, suitable for partial-range transitions, uses fewer parameters, and the μ(I) model, which is a purely fluid-like model, requires the least. Depending on the complexity and performance required, one can choose among these models for specific granular flow simulations.

6. Conclusions

In this study, we propose a novel unified phase transition constitutive model that integrates critical-state-based elastoplasticity with a modified kinetic theory accounting for particle stiffness. The model's performance is first evaluated under different factors such as concentration, particle stiffness, and strain rate paths through simple shear test simulations. Its effectiveness is further validated by simulating experimental data. Finally, the model is compared with two existing granular flow models, the μ(I) rheology model and the state-equation-based phase transition model, to highlight its unique contributions. The following conclusions are obtained:

(1) The developed elastoplasticity-based phase transition model effectively captures strain acceleration-dependent and particle stiffness-dependent characteristics through the collisional stress component. The increase in particle stiffness raises the collisional stress. Notably, the state variable, the granular temperature in the modified kinetic theory, can accurately describe the dependence on the strain rate path via the relation between $\dot{\gamma}^2$, which is consistent with experimental findings by Bagnold (1954).
(2) The developed phase transition model effectively captures concentration-dependent characteristics through both frictional and collisional stress components. The frictional stress model accurately represents the evolution of frictional stress from the initial state to the critical state for both loose and dense samples, while an increase in concentration enhances the collisional stress.
(3) During the transition from a solid-like to a fluid-like state, the dominant stress shifts from frictional to collisional, highlighting the model's capability to accurately capture the phase transition behavior. Validation through laboratory tests further confirms the effectiveness of the proposed elastoplasticity-based model

Table 4
The difference between the proposed model, state-equation-based phase transition model, and μ(I) model.

		Proposed elastoplasticity-based phase transition model (EPPTM)	State-equation-based phase transition model (SEPTM)	μ(I) model
Considering characteristics	Concentration-dependence	√	√	×
	Initial state to critical state	√	×	×
	Solid-like state	√	√	×
	Fluid-like state	√	√	√
Number of model parameter		18	12	5

(4) The comparative analysis reveals two implementations of critical state theory: (i) the proposed elastoplasticity-based phase transition model, which describes stress evolution from the initial state through the critical state to the fluid-like state, functioning as a full-range phase transition model; and (ii) the state-equation-based phase transition model, which describes stress evolution only from the critical state to the fluid-like state, serving as a partial-range phase transition model.
(5) The proposed elastoplasticity-based phase transition model and state-equation-based phase transition model well replicate the rheology of granular media, as the typical μ(I) granular flow model.
(6) The μ(I) model can be regarded as a purely fluid-like model, only describing the stress at the fluid-like state. It captures the rheological behavior in a simple form but does not consider concentration-dependent characteristics. The static friction coefficient μ_s in the μ(I) model may be equal to this coefficient at the critical state of the proposed model, while the dynamic friction coefficient μ_d may be equal to this coefficient of the collisional stress component in the proposed model.

CRediT authorship contribution statement

Hang Feng: Writing – review & editing, Writing – original draft, Validation, Software, Formal analysis, Data curation, Conceptualization. **Zhen-Yu Yin:** Writing – review & editing, Supervision, Methodology, Formal analysis, Conceptualization.

Declaration of competing interest

The authors declare that they have no known competing financial interests or personal relationships that could have appeared to influence the work reported in this paper.

Acknowledgments

This work was supported by the general research fund of the Research Grants Council (RGC) of the Hong Kong Special Administrative Region Government (HKSARG) of China (grant No. 15227923, 15229223, 15232224, T22-607/24-N).

Appendix A:. Critical-state-based elastoplastic stress part

This section describes the key features of the frictional stress part in the phase transition model see Yin et al., 2020; Feng et al., 2025). Following the theory of elastoplasticity, the strain increment is divided into an elastic part $\delta\varepsilon^e$ and a plastic part $\delta\varepsilon^p$:

$$\delta\varepsilon = \delta\varepsilon^e + \delta\varepsilon^p \tag{A1}$$

The elastic strain increment can be employed to obtain the stress increment via $\delta\sigma_f = \mathbf{K}_f : \delta\varepsilon^e$, in which $\mathbf{K_f}$ is a fourth-order stiffness tensor, is determined by the elastic modulus E_f and Poisson's ratio ν. The elastic modulus E_f is established by considering the nonlinear characteristics of granular media, expressed as:

$$E_f = E_0 p_{at} \frac{(2.97-e)^2}{(1+e)} \left(\frac{p_f}{p_{at}}\right)^n \tag{A2}$$

where p_{at} is the atmospheric pressure (i.e., $p_{at} = 101.3$ kPa); n is the Elastic constant controlling nonlinear stiffness; p_f is the hydrostatic part of frictional stress; e is the void ratio.

The yield function f_f is expressed as:

$$f_f = \frac{q_f}{p_f} - H_f \tag{A3}$$

where q_f is the deviatoric part of frictional stress; H_f is the hardening parameter, as follows:

$$H_f = \frac{M_p \varepsilon_d^p}{k_p + \varepsilon_d^p} \tag{A4}$$

where M_p is the slope of the failure line in the p_f-q_f plane, which is expressed as $M_p = 6sin\phi_c/(3-sin\phi_c)$ (where ϕ_c is the friction angle) in triaxial compression condition (Lode angle effect is introduced to follow the Mohr-Coulomb criterion). ε_d^p is the plastic deviatoric strain. k_p is a constant controlling the plastic hardening behavior.

The flow rule is developed to consider the stress dilatancy (contraction or dilation), expressed in explicit form:

$$\frac{\partial g}{\partial p_f} = A_d \left(M_{pt} - \frac{q_f}{p_f}\right), \frac{\partial g}{\partial q_f} = 1 \tag{A5}$$

where A_d is a parameter controlling the magnitude of the stress-dilatancy; M_{pt} is the transformation stress ratio corresponding to the transitional state between a contractive and a dilatant behavior. If the current stress ratio is smaller than M_{pt}, the material is contractive. Otherwise, it is dilative.

The critical state concept is incorporated into the frictional stress model by considering the critical void ratio, which is expressed as:

$$e_c = e_{\text{ref}} \exp\left[-\lambda\left(\frac{p_f}{p_{at}}\right)^{\xi}\right] \tag{A6}$$

where e_{ref} is the initial critical-state void ratio; λ is the slope of the critical state line (CSL) in the e-log p_f plane; parameter ξ controls the nonlinearity of CSL.

The critical-state theory is implemented in the frictional stress model by modifying the peak stress ratio M_p and phase transformation stress ratio M_{pt} via $M_p = 6sin\phi_p/\left(3-sin\phi_p\right)$ and $M_{pt} = 6sin\phi_{pt}/\left(3-sin\phi_{pt}\right)$, respectively. The peak friction angle ϕ_p and transformation angle ϕ_{pt} are expressed as:

$$\phi_p = \arctan\left[\left(\frac{e_c}{e}\right)^{n_p}\tan\phi_c\right] \tag{A7}$$

$$\phi_{pt} = \arctan\left[\left(\frac{e}{e_c}\right)^{n_d}\tan\phi_c\right] \tag{A8}$$

where n_p and n_d are parameters controlling the effect of particle interlocking.

Appendix B:. Auxiliary functions for collisional stress part

F, J, and Q are the auxiliary functions for collisional stress (Garzó and Dufty, 1999 ; Berzi and Jenkins, 2015; Vescovi et al., 2013).

$$F = \frac{1}{4G} + \frac{1+\varepsilon_n}{2} \tag{B1}$$

$$J = \frac{25\pi\eta^*}{768\Phi G} \tag{B2}$$

$$Q = \frac{5\pi\gamma^*}{128\Phi G} \tag{B3}$$

where η^* and γ^* are expressed as:

$$\eta^* = \eta^{\kappa^*}\left[1 + \frac{4}{5}\Phi G(1+\varepsilon_n)\right] + \frac{3}{5}\gamma^* \tag{B4}$$

$$\gamma^* = \frac{128}{5\pi}G(1+\varepsilon_n)\left(1 - \frac{1}{32}c^*\right) \tag{B5}$$

$$\eta^{\kappa^*} = \left(\nu_\eta^* - \frac{1}{2}\zeta^{0*}\right)^{-1}\left[1 - \frac{2}{5}(1+\varepsilon_n)(1-3\varepsilon_n)G\right] \tag{B6}$$

$$\zeta^{0*} = \frac{5}{12}g_0\left(1-\varepsilon_n^2\right)\left(1 + \frac{3}{32}c^*\right) \tag{B7}$$

$$\nu_\eta^* = g_0\left[1 - \frac{1}{4}(1-\varepsilon_n)^2\right]\left[1 - \frac{1}{64}c^*\right] \tag{B8}$$

$$c^* = 32(1-e_n)\left(1-2e_n^2\right)\left[81 - 17e_n + 30e_n^2(1-e_n)\right]^{-1} \tag{B9}$$

κ is the thermal conductivity; μ is the coefficient of the density gradient;

$$\kappa = \frac{4}{\sqrt{\pi}}d\rho GMT^{1/2} \tag{10}$$

$$\mu = \frac{25}{128}\sqrt{\pi}\,\frac{d}{\nu}NT^{3/2} \tag{11}$$

where M and N are the auxiliary functions, expressed as follows:

$$M = \frac{25\pi\kappa^*}{512\Phi G} \tag{12}$$

$$N = \mu^* \tag{13}$$

where κ^* and μ^* are expressed as:

$$\kappa^* = \kappa^{\kappa^*}\left[1 + \frac{6}{5}\Phi g_0(1+e_n)\right] + \left(\frac{16}{5}\right)^2\frac{\Phi^2 g_0}{\pi}(1+e_n)\left(1 + \frac{7}{32}c^*\right) \tag{14}$$

$$\mu^* = \mu^{\kappa^*}\left[1 + \frac{6}{5}\Phi g_0(1+e_n)\right] \tag{15}$$

$$\kappa^{\kappa^*} = \frac{2}{3}\left(\nu_\kappa^* - 2\zeta^{0*}\right)^{-1}\left(1 + \frac{1}{2}(1+p^*)c^* + \frac{3}{5}\Phi g_0(1+e_n)^2\left\{2e_n - 1 + \left[\frac{1+e_n}{2} - \frac{5}{3(1+e_n)}\right]c^*\right\}\right) \tag{16}$$

$$\nu_\kappa^* = \frac{1}{3}(1+e_n)g_0\left[1 + \frac{33}{16}(1-e_n) + \frac{19-3e_n}{1024}c^*\right] \tag{17}$$

$$\mu^{K^*} = 2\left(2\nu_\kappa^* - 3\zeta^{0*}\right)^{-1}\left\{\begin{array}{c}\left(1+\Phi\frac{g_0'}{g_0}\right)\zeta^{0*}\kappa^{\kappa^*} + \frac{p^*}{3}\left(1+\Phi\frac{p^{*\prime}}{p^*}\right)c^* \\ -\frac{4}{5}\Phi g_0\left(1+\frac{\Phi}{2}\frac{g_0'}{g_0}\right)(1+e_n)\left\{e_n(1-e_n) + \frac{1}{4}\left[\frac{4}{3} + e_n(1-e_n)\right]c^*\right\}\end{array}\right\} \tag{18}$$

ζ^* is the auxiliary function for the collisional dissipated energy, expressed as follows:

$$\zeta^* = \zeta^{0*} + \zeta^{1*} \tag{19}$$

$$\zeta^{0*} = \frac{5}{12} g_0 (1 - \varepsilon_n^2) \left(1 + \frac{3}{32} c^*\right) \tag{20}$$

$$\zeta^{1*} = \left[-\frac{5}{96} \frac{d(1+e)}{1} \sqrt{\frac{\pi}{T}} (1 - \varepsilon_n)(p^* - 1) + \frac{5}{32} (1 - \varepsilon_n^2) \left(1 + \frac{3}{64} c^*\right) g_0 C_d \right] \nabla \cdot \boldsymbol{u} \tag{21}$$

where C_d is expressed as:

$$C_d = \frac{5d(1+e)}{96} \sqrt{\frac{\pi}{T}} \frac{\frac{4}{15(1+e)} \lambda g_0 + (p^* - 1)\left(\frac{2}{3} - e_n\right) c^*}{\frac{1}{2}\zeta^{0*} + \nu_\gamma^* + \frac{5}{64} c^* \left(1 + \frac{3}{64} c^*\right) g_0 (1 - \varepsilon_n^2)} \tag{22}$$

$$\nu_\gamma^* = \frac{1 + \varepsilon_n}{48} g_0 \left[128 - 96\varepsilon_n + 15\varepsilon_n^2 - 15\varepsilon_n^3 + \frac{c^*}{64} (15\varepsilon_n^3 - 15\varepsilon_n^2 + 498\varepsilon_n - 434)\right] \tag{23}$$

$$\lambda = \frac{3}{8} \left[(1 - \varepsilon_n)(5\varepsilon_n^2 + 4\varepsilon_n - 1) + \frac{c^*}{12} (159\varepsilon_n + 3\varepsilon_n^2 - 19\varepsilon_n - 15\varepsilon_n^3) \right] \tag{24}$$

Data availability

Data will be made available on request.

References

Alaei, E., Marks, B., Einav, I., 2021. A hydrodynamic-plastic formulation for modelling sand using a minimal set of parameters. J. Mech. Phys. Solids 151, 104388.

Bagnold, R.A., 1954. Experiments on a gravity-free dispersion of large solid spheres in a Newtonian fluid under shear. Proc. R. Soc. Lond. A 225 (1160), 49–63.

Baumgarten, A.S., Kamrin, K., 2019. A general fluid–sediment mixture model and constitutive theory validated in many flow regimes. J. Fluid Mech. 861, 721–764.

Berzi, D., di Prisco, C.G., Vescovi, D., 2011. Constitutive relations for steady, dense granular flows. Phys. Rev. E-Statist., Nonlin. Soft Matter Phys. 84 (3), 031301.

Berzi, D., Jenkins, J.T., 2015. Steady shearing flows of deformable, inelastic spheres. Soft matter 11 (24), 4799–4808.

Bharathraj, S., Kumaran, V., 2018. Effect of particle stiffness on contact dynamics and rheology in a dense granular flow. Phys. Rev. E 97 (1), 012902.

Brewster, R., Silbert, L.E., Grest, G.S., Levine, A.J., 2008. Relationship between interparticle contact lifetimes and rheology in gravity-driven granular flows. Phys. Rev. E-Statist. Nonlin. Soft Matter Phys. 77 (6), 061302.

Carnahan, N.F., Starling, K.E., 1969. Equation of state for nonattracting rigid spheres. J. Chem. Phys. 51 (2), 635–636.

Chialvo, S., Sun, J., Sundaresan, S., 2012. Bridging the rheology of granular flows in three regimes. Phys. Rev. E-Statist., Nonlin. Soft Matter Phys. 85 (2), 021305.

Da Cruz, F., Emam, S., Prochnow, M., Roux, J.N., Chevoir, F., 2005. Rheophysics of dense granular materials: discrete simulation of plane shear flows. Phys. Rev. E-Statist., Nonlin. Soft Matter Phys. 72 (2), 021309.

Daniel, R.C., Poloski, A.P., Sáez, A.E., 2007. A continuum constitutive model for cohesionless granular flows. Chem. Eng. Sci. 62 (5), 1343–1350.

Drucker, D.C., Prager, W., 1952. Soil mechanics and plastic analysis or limit design. Q. Appl. Math. 10 (2), 157–165.

Dunatunga, S., Kamrin, K., 2015. Continuum modelling and simulation of granular flows through their many phases. J. Fluid Mech. 779, 483–513.

Dunatunga, S., Kamrin, K., 2022. Modelling silo clogging with non-local granular rheology. J. Fluid Mech. 940, A14.

Fei, M., Sun, Q., Xu, X., Jin, F., Zhou, G.G., 2016. Simulations of multi-states properties of granular materials based on non-linear granular elasticity and the MiDi rheological relation. Powder Technol. 301, 1092–1102.

Feng, H., Huang, M., Shi, Z., Shen, K., Wang, B., 2024b. Macro-element modeling of suction caisson subjected to vertical tensile loading via up-scaling soil stress-strain relations. Ocean Eng. 304, 117850.

Feng, H., Liang, W., Yin, Z., Hu, L., 2025. Material point method modeling of granular flow considering phase transition from solid-like to fluid-like states. Int. J. Numer. Anal. Methods Geomech.

Feng, H., Yin, Z.Y., Peng, M., 2024a. Macro-element modelling for lateral response of monopiles with local scour hole via hyperbolic hardening relation. Appl. Ocean Res. 153, 104233.

Garzó, V., Dufty, J.W., 1999. Dense fluid transport for inelastic hard spheres. Phys. Rev. E 59 (5), 5895.

MiDi, G.D.R., 2004. On dense granular flows. The Eur. Phys. J. E 14, 341–365.

Goldhirsch, I., 2008. Introduction to granular temperature. Powder Technol. 182 (2), 130–136.

Guo, X., Peng, C., Wu, W., Wang, Y., 2021. Unified constitutive model for granular–fluid mixture in quasi-static and dense flow regimes. Acta Geotech. 16, 775–787.

Huang, M., Chen, Z., Lu, X., 2018. Bifurcation prediction of shear banding in sand with non-coaxial critical state model considering inherent anisotropy. Soils Found. 58 (3), 641–653.

Hwang, H., Hutter, K., 1995. A new kinetic model for rapid granular flow. Contin. Mech. Thermodyn. 7, 357–384.

Jaeger, H.M., Nagel, S.R., Behringer, R.P., 1996. Granular solids, liquids, and gases. Rev. Mod. Phys. 68 (4), 1259.

Jenkins, J.T., Zhang, C., 2002. Kinetic theory for identical, frictional, nearly elastic spheres. Phys. Fluids 14 (3), 1228–1235.

Johnson, P.C., Jackson, R., 1987. Frictional-collisional constitutive relations for granular materials, with application to plane shearing. J. Fluid Mech. 176, 67–93.

Johnson, P.C., Nott, P., Jackson, R., 1990. Frictional-collisional equations of motion for participate flows and their application to chutes. J. Fluid Mech. 210, 501–535.

Jop, P., Forterre, Y., Pouliquen, O., 2006. A constitutive law for dense granular flows. Nature 441 (7094), 727–730.

Kamrin, K., 2010. Nonlinear elasto-plastic model for dense granular flow. Int. J. Plast 26 (2), 167–188.

Luding, S., 2016. So much for the jamming point. Nat. Phys. 12 (6), 531–532.

Lun, C.K., 1991. Kinetic theory for granular flow of dense, slightly inelastic, slightly rough spheres. J. Fluid Mech. 233, 539–559.

Marveggio, P., Redaelli, I., di Prisco, C., 2022. Phase transition in monodisperse granular materials: How to model it by using a strain hardening visco-elastic-plastic constitutive relationship. Int. J. Numer. Anal. Meth. Geomech. 46 (13), 2415–2445.

Nicot, F., Darve, F., 2005. A multiscale approach to granular materials. Mech. Mater. 37 (9), 980–1006.

Peng, C., Guo, X., Wu, W., Wang, Y., 2016. Unified modelling of granular media with smoothed particle hydrodynamics. Acta Geotech. 11, 1231–1247.

Redaelli, I., di Prisco, C., 2019. Three dimensional steady-state locus for dry monodisperse granular materials: DEM numerical results and theoretical modelling. Int. J. Numer. Anal. Meth. Geomech. 43 (16), 2525–2550.

Roscoe, K., Schofield, A., Thurairajah, A., 1963. Yielding of clays in states wetter than critical. Geotechnique 13 (3), 211–240.

Redaelli, I., Di Prisco, C., Vescovi, D., 2016. A visco-elasto-plastic model for granular materials under simple shear conditions. Int. J. Numer. Anal. Meth. Geomech. 40 (1), 80–104.

Savage, S.B., 1984. The mechanics of rapid granular flows. Adv. Appl. Mech. 24, 289–366.

Savage, S.B., Sayed, M., 1984. Stresses developed by dry cohesionless granular materials sheared in an annular shear cell. J. Fluid Mech. 142, 391–430.

Schofield, A., Wroth, P., 1968. Critical State Soil Mechanics.

Singh, A., Magnanimo, V., Saitoh, K., Luding, S., 2015. The role of gravity or pressure and contact stiffness in granular rheology. New J. Phys. 17 (4), 043028.

Torquato, S., 1995. Nearest-neighbor statistics for packings of hard spheres and disks. Phys. Rev. E 51 (4), 3170.

Vescovi, D., 2014. Granular shear flows: constitutive modeling and numerical simulations (Thesis).

Van der Vaart, K., Rahmani, Y., Zargar, R., Hu, Z., Bonn, D., Schall, P., 2013. Rheology of concentrated soft and hard-sphere suspensions. J. Rheol. 57 (4), 1195–1209.

Vescovi, D., di Prisco, C., Berzi, D., 2013. From solid to granular gases: the steady state for granular materials. Int. J. Numer. Anal. Meth. Geomech. 37 (17), 2937–2951.

Vescovi, D., Luding, S., 2016. Merging fluid and solid granular behavior. Soft Matter 12 (41), 8616–8628.

Wang, Y., Wu, W., 2024. Hypoplastic model for solid-like and fluid-like granular flows. Comput. Geotech. 172, 106466.
Wood, D.M., 1990. Soil Behaviour and Critical State Soil Mechanics.
Wu, W., Bauer, E., 1994. A simple hypoplastic constitutive model for sand. Int. J. Numer. Anal. Meth. Geomech. 18 (12), 833–862.
Wu, W., Lin, J., Wang, X., 2017. A basic hypoplastic constitutive model for sand. Acta Geotech. 12, 1373–1382.
Wu, W., Wang, S., Alipour, M., 2020. Constitutive modelling for fast granular flow. In ALERT Doctoral School 2020 Point Based Numerical Methods in Geomechanics (pp. 69-88).
Yin, Z.Y., Hicher, P.Y., Jin, Y.F., 2020. Practice of constitutive modelling for saturated soils. Springer Singapore.
Zhang, P., Yin, Z.Y., Jin, Y.F., Liu, X.F., 2021. Modelling the mechanical behaviour of soils using machine learning algorithms with explicit formulations. Acta Geotech. 1–20.
Zhang, P., Yin, Z.Y., Jin, Y.F., Ye, G.L., 2020. An AI-based model for describing cyclic characteristics of granular materials. Int. J. Numer. Anal. Meth. Geomech. 44 (9), 1315–1335.
Zhu, C., Peng, C., Wu, W., 2022. Lagrangian meshfree particle method (SPH) based simulation for granular flow in a rotating drum with regularized μ(I) elastoplastic model. Powder Technol. 408, 117699.